


## Microstructure analysis and image-based modelling of face masks for COVID-19 virus protection

Wenjia Du <sup>1</sup>, Francesco Iacoviello <sup>1</sup>, Tacson Fernandez<sup>2</sup>, Rui Loureiro<sup>2,3</sup>, Daniel J. L. Brett<sup>1</sup> & Paul R. Shearing <sup>1</sup>✉

SARS-CoV-2 may spread through respiratory droplets released by infected individuals. The viruses are transmitted in moist droplets which cause coronavirus disease. Many countries have mandated the wearing of face masks, to various extents. However, the efficacy of masks is yet to be well rationalised given the limited microstructure information. Here, three common face masks and associated air permeations were revealed by coupling X-ray tomographic imaging and infrared thermal imaging techniques. Quantitative parameters have been extracted from the 3D images. Also, image-based modelling was performed to simulate the permeability to show how droplets pass through the porous structure. Our results show that the N95 mask has the smallest average pore diameter ( $\sim 30\mu\text{m}$ ) and the densest nanoscale fibres which provides superior droplet filtration among all cases. Modifications to the N95 masks are proposed to develop the next generation mask with higher efficacy and better breathability.

<sup>1</sup>The Electrochemical Innovation Lab, Department of Chemical Engineering, University College London, London, UK. <sup>2</sup>Royal National Orthopaedic Hospital, Brockley Hill, Stanmore, Middlesex, UK. <sup>3</sup>Department of Orthopaedics and Musculoskeletal Science, University College London, London, UK. ✉email: [p.shearing@ucl.ac.uk](mailto:p.shearing@ucl.ac.uk)

The rapid spread of SARS-CoV-2 in early 2020 has led to a coronavirus disease (COVID-19) pandemic globally, posing an unprecedented threat to individual health, national health systems, economies as well as social stability<sup>1,2</sup>. Until March 2021, around 120 million infected cases and over 2.6 million deaths have been reported worldwide<sup>3</sup>.

To mitigate COVID-19 transmission, many countries were forced to introduce strict measures including travel restrictions, schools and non-essential businesses closure and limitations on public gatherings<sup>4</sup>. The authorities introduced such measures to minimise person-to-person exposure, thus reducing the disease transmission<sup>5</sup>. Moreover, individual activities such as keeping social distance, self-isolation, frequent handwashing, disinfecting surfaces and wearing a face mask are also required to further curtail transmission<sup>6</sup>. Many countries imposed tougher rules on mask wearing, such as Singapore mandating the wearing of face masks outside of the home in June 2020<sup>7</sup>. Almost at the same time, the WHO announced that face masks are recommended for use by the general public<sup>8</sup>.

Recent investigations have implied that masks help to reduce the disease transmission and therefore slow down the growth of the epidemic curve<sup>9–11</sup>. However, there are still ongoing debates on the efficacy of wearing masks<sup>12–14</sup>. Inevitably, an individual might be confused by misleading information and even advised against wearing a mask during COVID-19 pandemic<sup>15</sup>. This might be attributed to two main reasons; (1) both infection source and pathways for COVID-19 transmission are not yet fully understood by virologists; (2) there is a general lack of information relating to the material structure of commonly used face masks.

It was widely considered that the filtration performance of a face mask is determined by its microstructure (such as fibre diameter, thickness, porosity), surface charge density and environmental conditions (air velocity, aerosol particle diameter, temperature and humidity)<sup>16</sup>. Fischer, et al<sup>17</sup> reported a low-cost optical measurement of droplets filtering for common masks. Aydin, et al<sup>18</sup> used a high-speed camera to evaluate the droplet blocking efficiency for 11 household masks, and they suggested using the multiple fabric layers may help reduce droplet transmission of respiratory infections. However, the aforementioned studies are mainly focused on mask performance, there is very limited information relating to mask microstructures. Previous investigations<sup>19,20</sup> are intrinsically limited to 2D observation and cannot provide spatial information. Very recently, Lee, et al<sup>21</sup> characterised nano fabrics with adherent NaCl particles within the N95 filter layer using X-ray tomography. Unfortunately, no comprehensive microstructure investigations on various, widely utilised face mask types have been reported to date. The relationship between the micro- and nano- fibrous structures and their performance (filtration efficacy and breathability) are yet to be rationalised due to limited reports in the literature.

In this paper, we have studied three common types of face masks (see Supplementary Fig. 1) by correlative application of X-ray computed tomography (CT) and infrared (IR) thermal imaging techniques. We have used high-resolution (350 nm) micro-scale X-ray tomography to observe the 3D microstructures of fibres and related pore networks. Microstructural parameters have been comparatively quantified via skeletonization and pore network modelling (PNM). Using obtained 3D datasets, we have performed image-based simulations to comparatively study the flow of respiratory droplets that pass through the different porous materials. Our results show that the mixture of micro- and nano-fibres are able to improve the filtration efficacy. Longer microscale fibres could directly block the droplets, whereas the shorter nanoscale fibres help to reduce the pore size and increase the specific surface area that will be a benefit for small particles

(<200 nm) absorption. We found that a reusable mask has the best breathability and comfort whereas the N95 mask provides the best aerosol filtration. We have made the data freely available to the scientific community and to the general public in order to help develop better filtration devices and face masks and to aid wider public understanding.

## Results

**3D morphology and structure of face masks.** The microstructure and morphology of three commercial face masks obtained via high-resolution X-ray tomography at submicron scale are illustrated in Fig. 1 and Supplementary Movie 1. We exclusively presented 3D microstructures of the three masks reconstructed by advanced reconstruction algorithm, namely, reusable mask (Fig. 1a–c), surgical mask (Fig. 1d–f) and N95 mask (Fig. 1g–i). The details of both standard and advanced iterative reconstruction (Supplementary Fig. 2 and Supplementary Note 1) can be found in the supplementary materials. Basically, there are two phases, i.e., fibres and air (indicated by a white arrow) in each sample according to the contrast of grayscale values. Both micro- and nano- fibres are observed in the surgical and N95 masks from X–Y and X–Z slices (first and second rows of Fig. 1) selected in the middle of 3D volume. Although the same structural characteristics can be observed via SEM (Supplementary Fig. 3), results are intrinsically limited to the surface in 2D. The interior information beneath the surface can only be revealed by 3D tomography techniques which reveal the connectivity and therefore the percolation behaviour of the mask material. The reusable mask has a single layer morphology polymerised by coarser fibres (Fig. 1b), while the surgical mask exhibits a sandwich structure which includes three layers within the field of view (FOV, highlighted by yellow dashed lines in Fig. 1e). To achieve the same highest resolution for the filter layer in N95 mask, two layers (instead of three) are only captured because of the limited FOV (Fig. 1h).

Correspondingly, 3D microstructures of these three masks are rendered in purple, green and yellow (third column, Fig. 1). The same colour but different transparent values are used to distinguish multiple layers for the surgical and the N95 masks. The air phase is deliberately transparent to visualise the fibres for all cases. In Fig. 1c, the reusable mask shows large gaps between neighbouring micro-fibres ranging from tens to hundred micrometres at the bottom part of the sample. In contrast, for the surgical mask in Fig. 1f, the middle melt-blown layer (Layer #2) is composed of micro- and nano- fibres, where the fibre density is clearly higher than the other two exterior layers (Layer #1 and #3). This middle layer, with a thickness of ca.100  $\mu\text{m}$ , usually plays a crucial role in filtering microbes from crossing the surgical mask. Similarly, we observed a filter layer with a thickness of ca. 250  $\mu\text{m}$  (Layer #b, orange dashed line in Fig. 1i) composed by a large portion of nano-fibrous structures in N95 mask. The thickness of this filtered layer in N95 is usually about 200–400  $\mu\text{m}$  according to ref. <sup>21</sup>. In addition, the Layer #b is covered by a shield-like layer (Layer #a) with a thickness of ca. 80  $\mu\text{m}$  (Fig. 1i). Also, the diameter of the nano-fibres in N95 mask is clearly smaller than those in the surgical mask (Fig. 1f, i and Supplementary Fig. 3b, c) confirmed by SEM and X-ray imaging.

The volumetric parameters have been extracted from the 3D images (Table 1). For the crucial layers in each mask, the volume fractions of porosity ( $V_{f\text{-porosity}}$ ) are 82% (reusable layer), 69% (surgical Layer 2), and 86% (N95 Layer #b). We noticed that the Layer #a, act as exterior layer of N95 mask, has the shield-like structure (Fig. 1i) with less porosity (44%). There is small fraction (ca.1%) of particles in N95 sample. The volume fraction of fibre ( $V_{f\text{-fibres}}$ ) for all masks is usually less than 30%. Regarding to

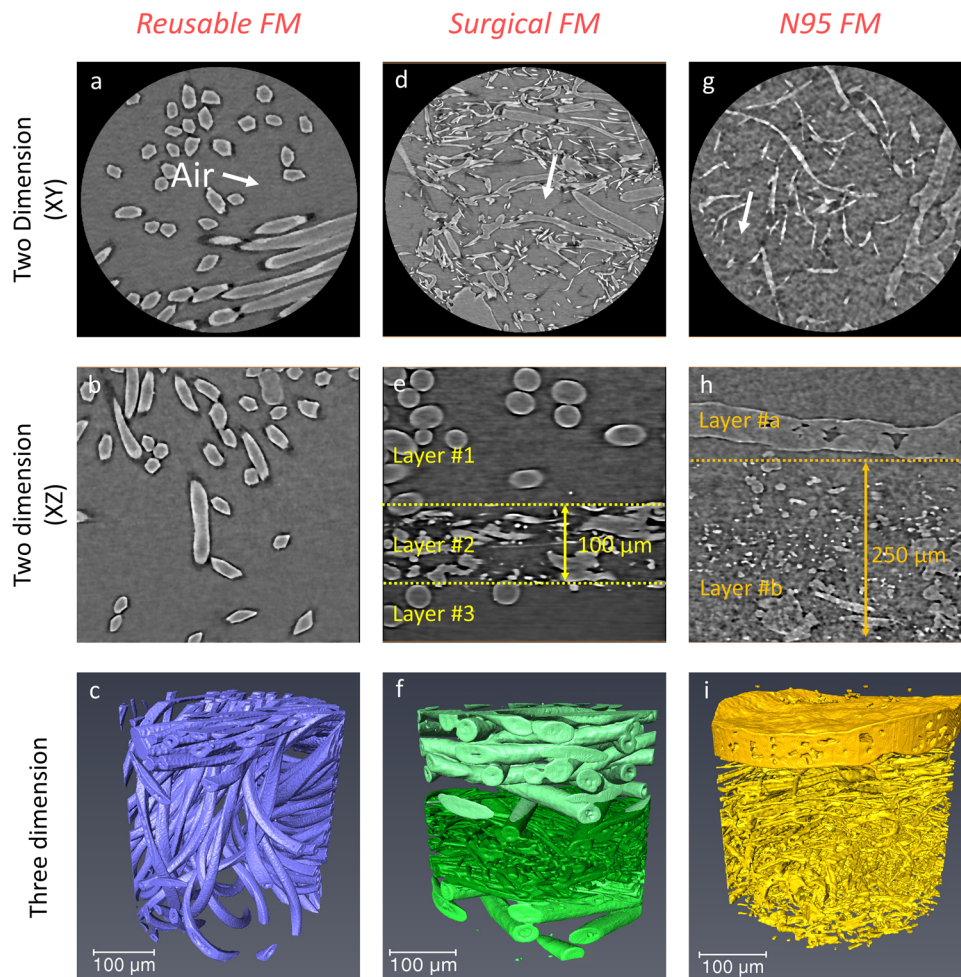


**Fig. 1** 3D microstructures of the three commercial face masks (FMs) obtained by high-resolution X-ray tomography. The X-ray micro-CT images of the reusable (a–c), surgical (d–f) and N95 (g–i) face masks are reconstructed by using advanced iteration algorithm. The extracted cross-sectional slices in the X–Y (a, d, g) and X–Z (b, e, h) planes (X-ray attenuation depicted through a grayscale) show that each sample has two phases, namely fibres and air. The surgical face mask has three layers within the FOV whereas two layers are observed in N95. 3D microstructures of the reusable (c), surgical (f) and N95 (i) face masks are rendered (removing the pore phase) in purple, green and yellow, respectively.

**Table 1** The quantification of volume fraction and specific surface area extracted from the reusable, surgical and N95 face masks.

Specimens	Phase volume fraction [%]			Surface area per volume [ $\mu\text{m}^2 \mu\text{m}^{-3}$ ]		
	Fibre	Air	Particle	Fibre	Air	Particle
Reusable	18	82	-	0.27	0.08	-
Surgical Layer #1	26	74	-	0.17	0.09	-
Surgical Layer #2	31	69	-	0.40	0.18	-
Surgical Layer #3	12	88	-	0.21	0.07	-
N95 Layer #a	55	44	1	0.10	0.20	1.73
N95 Layer #b	14	86	-	0.64	0.14	-

mixture of nano- and micro- fibres, the N95 mask has highest specific surface area ( $S_{\text{area-N95}} = 0.64$ ) than the surgical mask ( $S_{\text{area-surgical}} = 0.40$ ) and the reusable mask ( $S_{\text{area-reusable}} = 0.27$ ).

PNM is performed for a better understanding of pores distribution on the droplet transmission (Fig. 2 and Supplementary Movie 2). The visualisations (first and second columns) and pore diameter ( $\Phi_{\text{pore}}$ ) distribution (third column) of the reusable

mask (Fig. 2a–c), the surgical mask (Fig. 2d–f) and the N95 mask (Fig. 2g–i) are presented. To verify the accuracy of the PNM and provide an overview of the arrangement and distribution of the pores, 3D fibrous structures are manually overlapped with pores as shown in the first column of Fig. 2. The spheres and cylinders represent pores and throats (second column), respectively. All spheres (the radius of pores ranges from 0 to 50  $\mu\text{m}$ ) and throats are automatically assigned with different colours according to their equivalent radius to indicate the porosity and pore connectivity. For instance, spheres with the largest diameter were marked in red whereas those with the smallest diameter were labelled in blue. In Fig. 2b, for the reusable mask, nearly 12 larger spheres ( $\Phi_{\text{pore}} > 60 \mu\text{m}$ ) occupy most of the sample volume and there are few neighbouring smaller pores. The percentages of the largest pores ( $\Phi_{\text{pore}} > 90 \mu\text{m}$ ) are ca. 10% (reusable mask, Fig. 2c) and ca. 2.5% (surgical mask, Fig. 2f), respectively. By contrast, for the N95 mask (Fig. 2h, i), there are no pores (labelled in either yellow or red) where the diameter is larger than 65  $\mu\text{m}$  in the FOV. Instead, nearly 50% spheres are smaller than 30  $\mu\text{m}$  and, they are homogeneously distributed in same FOV. Interestingly, in the sandwich structure of the surgical mask, the spheres exhibit a similar characteristic (Fig. 2e). Specifically, the sphere size in the interior layer (layer #2) seems considerably smaller ( $\Phi_{\text{pore}} < 15\text{--}30 \mu\text{m}$ ) than those in the exterior layers (Layer #1 and #3).

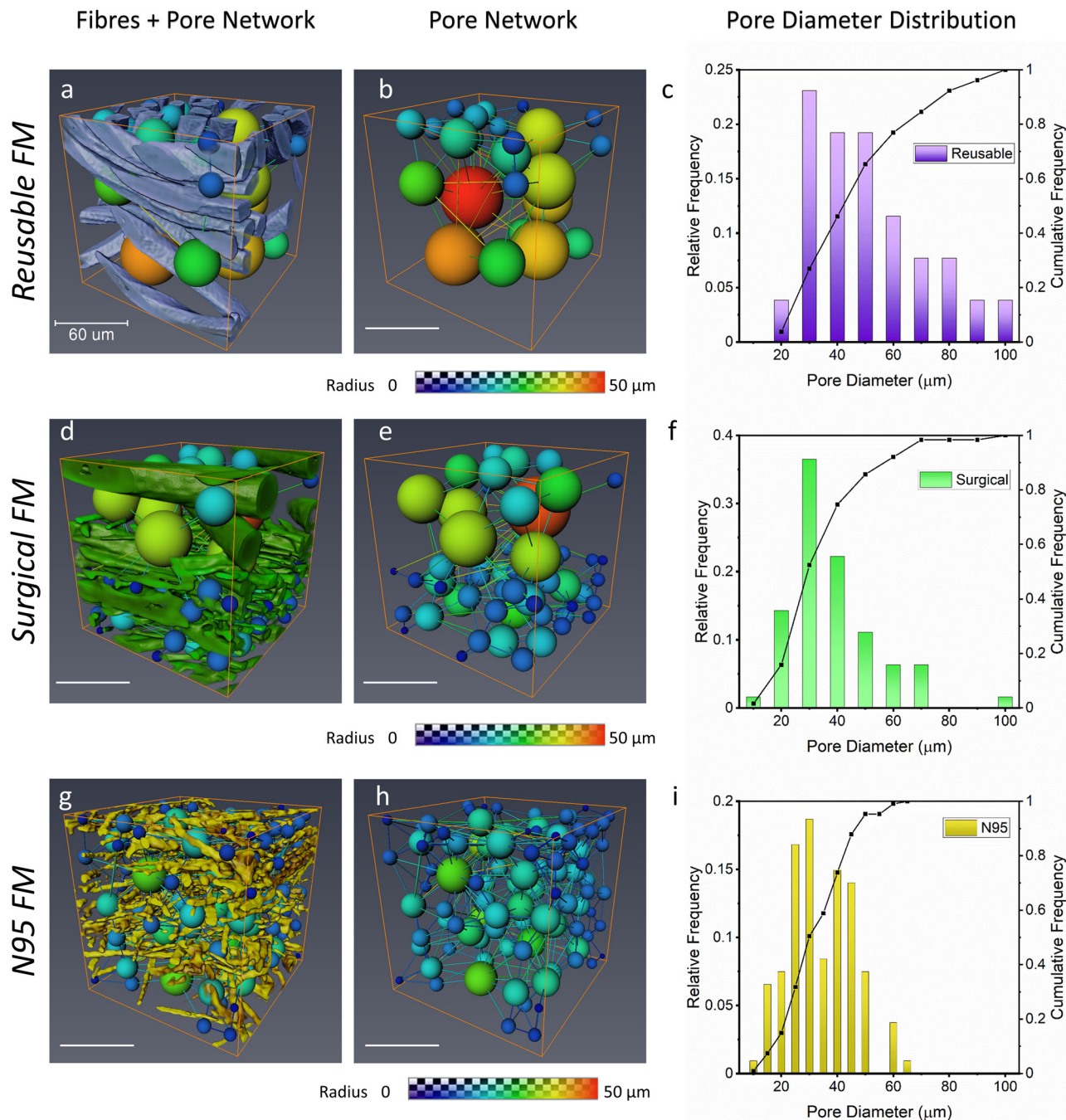


**Fig. 2 The pore networks modelling (PNM) of the three commercial face masks and their pore diameter distribution.** The air phase (as shown in Fig. 1) is represented as a series of spheres connected by narrower throats (shown as lines). The assigned-colour spheres represent pores scaled according to their equivalent radius (in the range of 0–50 μm). The fibres superimposed with pore networks are shown in **a, d, g** the pores and throats **b, e, h** indicate the porosity within the sample volume. The associated pore diameter distributions **c, f, i** are quantified to evaluate the droplets filtration efficiency when cough or sneezing.

Furthermore, the results demonstrate that the reusable mask has the widest pore diameter domain ranging from 20 to 100 μm, whereas the N95 has pores from 10 to 65 μm. In Supplementary Fig. 4f, the average pore diameter for the reusable mask, surgical mask and N95 mask are ~47, ~33 and ~30 μm, respectively.

Figure 3 and Supplementary Movie 3 show the visualisation of traced skeletons for three face masks. The 3D fibres are rendered as 70% of transparency with their skeletons inside (first column). The skeletons (second column) are used to represent each individual fibre for further quantification while 3D fibres are deliberately masked. Skeletons (curved lines) are scaled according to their length ( $L_{\text{fibre}}$ )

and labelled with different colours (ranging from 50 to 750 μm, lines shorter than 50 μm were ignored). Such length measurements via skeletonization based on 3D imaging provide valuable microstructural quantification. The minimum and maximum values of  $L_{\text{fibre}}$  and correlated  $\Phi_{\text{pore}}$  in each face mask cases are summarised in Table 2 for future comparative study. The length distributions of fibre (third column of Fig. 3) are quantified to understand fibrous morphology. In Fig. 3c, over 20% of fibres of the reusable mask are longer than 400 μm and their maximum length is up to 750 μm. By contrast, for the N95 case, ca.20% of fibres are over 200 μm and there are no fibres that are longer than 500 μm (Fig. 3i). The average

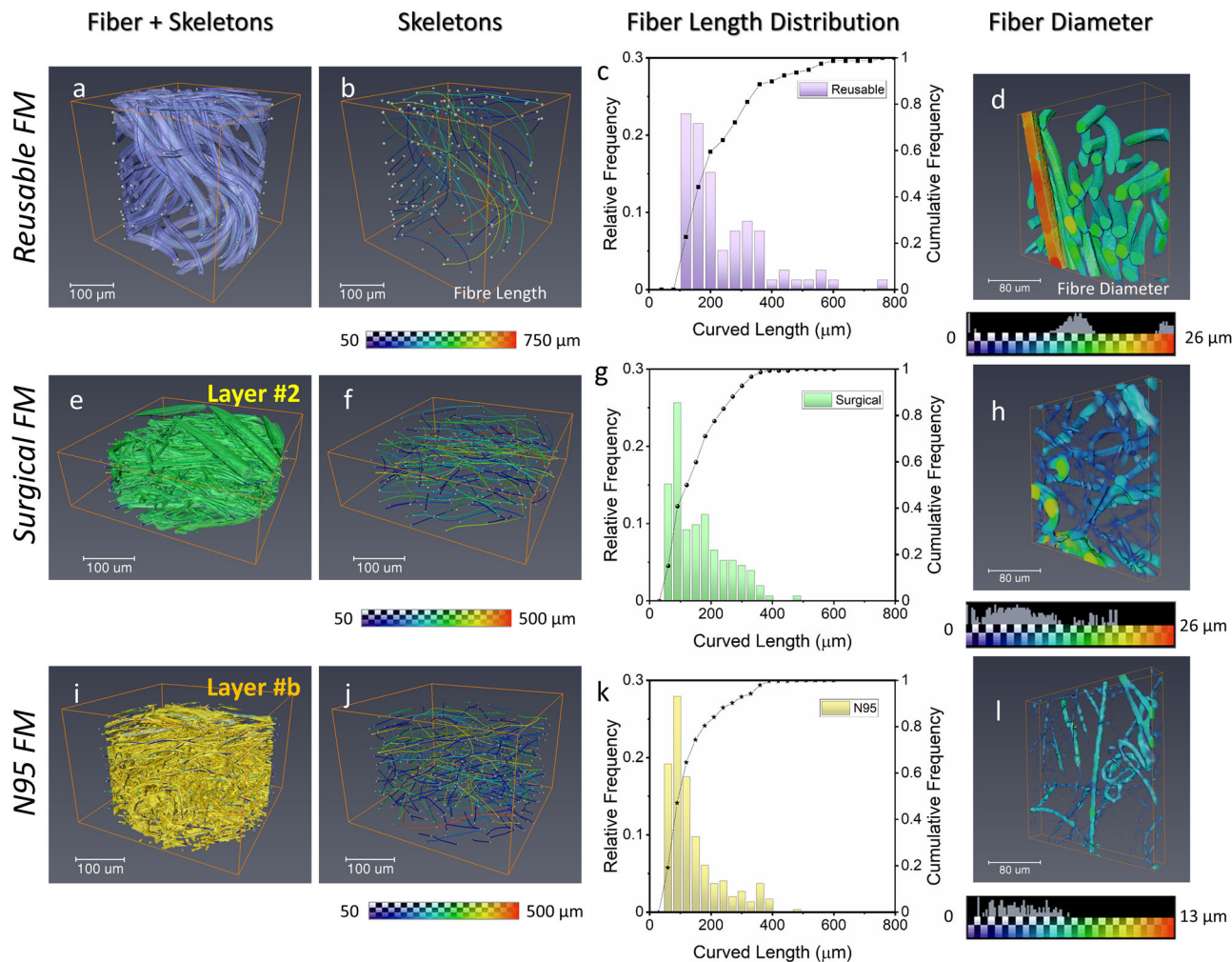


**Fig. 3 The quantification of fibres (length and diameter) of the three commercial face masks.** The interactive fibre tracing and its correlation algorithms (skeletonizations), and thickness mapping are performed in Avizo to understand face masks microstructure, and performance. **a, e, i** 3D fibres are rendered as transparent (70%) with their skeletons inside. **b, f, j** The skeletons (curved lines) are used to track and represent each individual fibre. True fibres are deliberately masked. Skeletons are labelled to different colours (range from 50 to 750  $\mu\text{m}$ , skeletons shorter than 50  $\mu\text{m}$  are ignored) according to their length scale. **c, g, k** The corresponding length distributions of fibres are quantified. **d, h, l** The diameter of fibres is assigned to multiple colours that scaled is according to the fibre thickness. It should be noted that the thickness distributions are displayed above the colour bar.

**Table 2 The quantification of fibre length ( $L$ ) and correlated pore size ( $\Phi$ ) using the skeletonization and pore-network modelling modules.**

	Reusable mask	Surgical mask	N95 mask
Number of fibres	78	151	296
Minimum curved length ( $\mu\text{m}$ )	81	50	48
Maximum curved length ( $\mu\text{m}$ )	751	463	454
Number of pores	25	62	106
Minimum pore diameter ( $\mu\text{m}$ )	20	10	8
Maximum pore diameter ( $\mu\text{m}$ )	98	92	64

Their average values are plotted in Supplementary Fig. 4.

lengths for three masks (Supplementary Fig. 4d) validate prior 3D observation (Fig. 1), showing the reusable mask has the longest fibre length (ca. 219  $\mu\text{m}$ ), followed by the surgical mask of ca. 143  $\mu\text{m}$ , and N95 fibre has the shortest fibre (ca. 126  $\mu\text{m}$ ). Moreover, the fibre diameter ( $\Psi_{\text{fibre}}$ ) results (fourth column) confirms our prior

observations (Fig. 1), showing the reusable mask (Fig. 3d) has the largest average diameter of fibres ( $\Psi_{\text{fibre-Reusable}} = 13.8 \mu\text{m}$ ), while the N95 mask (Fig. 3i) has the finest fibre ( $\Psi_{\text{fibre-N95}} = 2.2 \mu\text{m}$ ). Although  $\Psi_{\text{fibre-N95}}$  obtained by X-ray CT is comparable with results that from our SEM and previous studies<sup>16,21</sup>, measuring  $L_{\text{fibre}}$  by X-ray CT is considered more reliable than that by SEM because measuring curved fibres will need another dimension (z-axis).

**The aerosol permeability.** Permeability ( $\chi$ ) indicates the flow ability through porous materials. This helps to understand how aerosol containing bacteria and coronaviruses penetrates the mask, thus evaluating the air filtration performance of the three face masks. The permeability of three different masks along the Z-axis direction is shown in Fig. 4 and Supplementary Movie 4, which are the normal airflow direction of masks. The associated permeability values are summarised in Table 3. The virtual streamlines (second row) are simulated to reveal the ejected aerosol flow pathways, scaled according to their relative velocity. The fibre structures are deliberately superimposed with the flow streamlines (first row, Fig. 4) to visualise where and how the flow is blocked by the fibres. The reusable mask (Fig. 4a, d) has the lowest flow resistance, and the

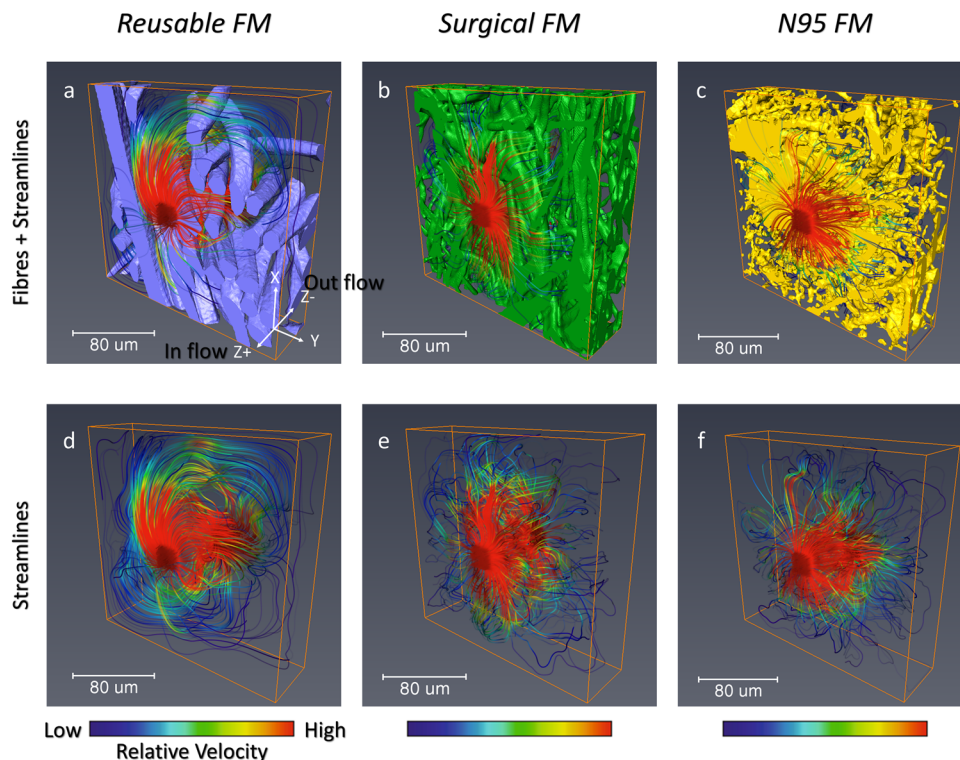


**Fig. 4** Visualisation of the illuminated streamlines of the three face masks representing the velocity field in the permeability simulation. The fibre structures are superimposed with the flow streamlines **a–c** to visualise where and how the flow is blocked by the fibres. The streamlines **d–f** are displayed to reveal the virtual ejected aerosol flow pathways, scaled according to their relative velocity.

**Table 3** The absolute permeabilities of reusable, surgical and N95 face masks within the sub-volume domain at Z-axis directions.

Direction	Permeability [ $\mu\text{m}^2$ ]		
	Reusable FM	Surgical FM	N95 FM
Z-axis	0.37	0.34	0.26

It should be noted that the Z-axis is normal to the mask plane (the Z-axis is the direction..... when mask wearer breath air in and out).

homogeneous distribution of flows at the outlet direction (Z-) has the highest relative velocity among all cases. We noticed that the nanoscale fibres may decrease the flow velocity (Fig. 4b, c). For example, the N95 mask (Fig. 4f) has the most heterogeneous flow at the outlet plane. Table 3 shows the permeability has a sequence of  $\chi_{\text{reusable}} > \chi_{\text{surgical}} > \chi_{\text{N95}}$ , suggesting that the higher air permeability in reusable mask will have lower blocking efficiency. Hence, droplets will have the slowest diffusion procedure in N95 mask which agrees with 3D streamline visualisations.

**Real-time IR thermal imaging.** Ideally, an excellent face mask will bring good air permeation and comfort to the mask wearer whilst providing adequate protection. The IR thermal camera can detect microwave with wavelengths from 1 to 7.5  $\mu\text{m}$ , and it can be used as a complementary method to quickly evaluate the air filtration of face masks, because the transmission of oxygen ( $\text{O}_2$ ), carbon dioxide ( $\text{CO}_2$ ) and moisture will be revealed by the IR camera. The temperatures in each case can be tracked by mapping. In Fig. 5, the real-time thermography shows images with a range of measured temperature ( $T$ ) from 20.2 to 33.6  $^{\circ}\text{C}$ . The yellow colour represents the warmer region (correspond to high air filtration) while darker purple indicates the cooler region

(correspond to low air filtration). These thermal images were taken when the mask wearer breaths in (upper row) and out (lower row) wearing the reusable (first column), surgical (second column) and N95 (third column) masks. Clearly, both the reusable mask (Fig. 5b) and the surgical mask (Fig. 5d) exhibit better breathing comfort than the N95 mask (Fig. 5f) as higher temperatures were observed at the facial area (white dash circle). The N95 has coldest temperature, indicating the moisture transmission is the lowest among all samples.

## Discussion

A series of morphological parameters can be extracted from 3D images (Fig. 1). For instance, the specific surface areas, phases volume fraction, pores diameter, as well as length and diameter of fibres are presented in Figs. 2, 3, Tables 1, 2 and Supplementary Fig. 4. These values play a decisive role in determining mask performance, such as breathability and filtration. For simplicity, we obtained overall porosity for the surgical and N95 mask by calculating an average value of multiple layers. Our results show that the reusable mask has highest porosity (82%), and the surgical mask has an intermediate value (77%). The N95 mask displays the lowest porosity (65%). Basically, higher porosity allows air in and out and thus will have higher breathability. Both porosity fraction (86%) and fibre diameter in our N95 mask are comparable to Lee's investigation<sup>21</sup> using the same X-ray CT scanner, demonstrating that X-ray imaging generates credible data with high repeatability.

The porosity can be extracted into a Pore Network Model by using a largest ball fitting through a given pore<sup>22</sup>, paving a new and direct approach to evaluate the droplet filtration efficiency. Traditionally, the pore size can be measured by the physical measurements via mercury intrusion porosimetry (MIP). However, the MIP could not accurately measure the air filled pores because this method does not depend solely on the actual pore size distribution. Instead, additional conditions need to

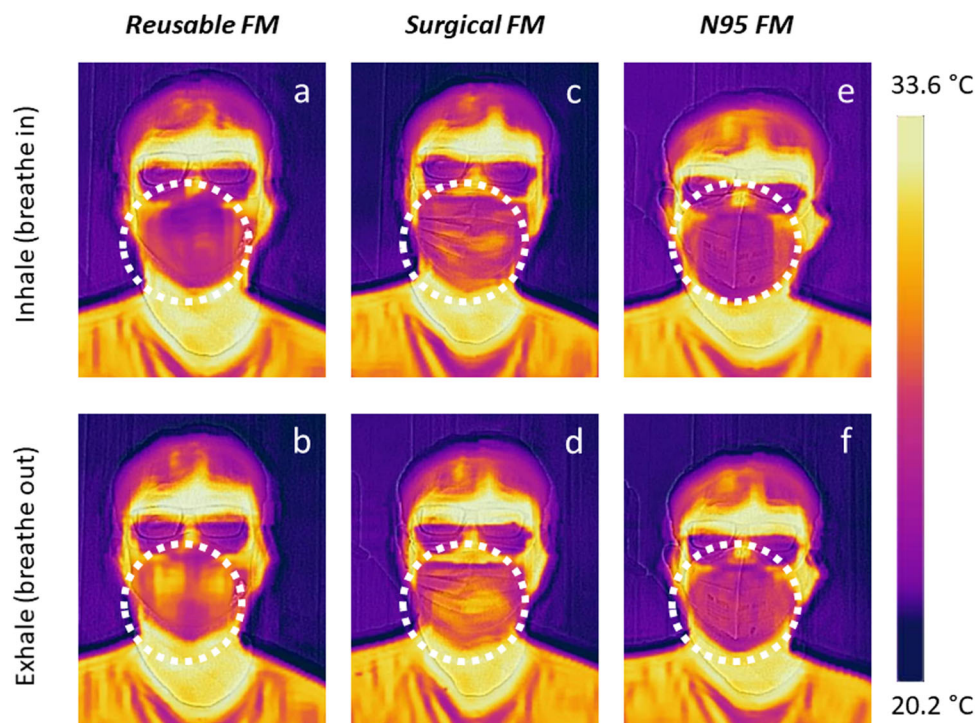


**Fig. 5** Evaluation of air transmission ( $\text{O}_2$  and  $\text{CO}_2$ ) level for three associated face masks by infrared thermal imaging. The thermal images of  $\frac{3}{4}$  portrait are acquired when volunteer breath in (a, c, e) and out (b, d, f) wearing the reusable (a–b), surgical (c–d) and N95 (e–f) face masks, respectively.

be considered such as the total volume of intruded mercury. The smallest pore measured by the MIP is at least one order of magnitude smaller than that of direct image analysis. Also, the MIP data requires a model (i.e., Washburn equation) to estimate the pore size and very few real materials actually fulfil the requirements of the model<sup>23,24</sup>. Hence, X-ray tomographic imaging is a non-destructive, alternative approach to characterise the pore distribution in the materials<sup>25</sup> and, the same pore extraction approach (PNM in this manuscript) has been widely and successfully applied in other research communities<sup>26,27</sup>.

On one hand, the pore size distributions (third column of Fig. 2) show that the N95 filter has porous constitution with lots of small pores, whereas reusable filter has the opposite trend. The average pore size has the following trend  $\Phi_{\text{pore-Reusable}} > \Phi_{\text{pore-Surgical}} > \Phi_{\text{pore-N95}}$ . On the other hand, the droplets released by sneezing, coughing, typically have droplet size between  $\sim 40 \mu\text{m}$  to  $\sim 1 \text{mm}$ <sup>28–31</sup>. The viruses are transmitted in moist droplets; most droplets are heavy enough to fall within 2 m or so, therefore individuals within that distance will be exposed to viruses<sup>32,33</sup>. By comparing the documented droplet diameter distributions during sneezing in ref. 28 with the pore diameter distribution in this experiment (Supplementary Fig. 5), it is obvious to see that peak of pore distribution for the reusable mask (from 20 to  $100 \mu\text{m}$ , peak at  $45 \mu\text{m}$ ) is close to the peak region of droplet diameters (range from 40 to  $1000 \mu\text{m}$ , first peak at  $100 \mu\text{m}$ ), leading to a larger overlapped area. By contrast, the peak of the pore diameter distribution for the N95 mask (from 10 to  $65 \mu\text{m}$ , peak at  $30 \mu\text{m}$ ) is further away from droplet peak, having much less overlapping area. In summary, we have demonstrated that with the smallest pore diameter among all specimens the N95 has the best filtration efficiency to prevent droplets transmission.

We further study the reason why N95 mask has best filtration efficacy than other two masks by closely examining the internal structure. Firstly, the shield-like structure Layer #a acts as the first barrier for preventing macroscale droplets (up to  $100 \mu\text{m}$ ) and reducing

the droplet momentum. However, this prevents the air transmission due to its less porous structure ( $V_{\text{F-porosity-Layer \#a}} = 44\%$ ) and thus leads to lower breathability. Secondly, the diameters of microscale droplets ( $\Phi_{\text{droplet}} > 40 \mu\text{m}$ ) are found to be larger than pore diameter within N95 ( $\Phi_{\text{pore}} = 30 \mu\text{m}$ ). Under this condition, most droplets are likely to be trapped by nanoscale fibre in Layer #b via impaction, interception and diffusion (Supplementary Fig. 6) as the droplet size is larger than the fibre spacing. Thirdly, the surface area value of Layer #b ( $S_{\text{area-N95}} = 0.64$ ) is significantly higher than the other two masks (Table 1). Those nano-fibres with the largest surface area will have more opportunities to capture the smaller droplets ( $\Phi_{\text{droplet}} < 200 \text{nm}$ ) on their surface via electrostatic attraction<sup>34</sup>. These multiple nano- and micro-fibre layers could capture microscale droplets before they evaporate into nano particles. Hence, the filtration can be improved by increasing the thickness of Layer #b without losing the breathability due to higher porosity ( $V_{\text{F-porosity-Layer \#b}} = 86\%$ ). Moreover, the embedded nanoscale particle (1%) within the N95 mask may further reduce the fibre spacing and enhance electrostatic attraction. Since mask fibres are the main regulating factor for droplet capture, we speculate that fibres with longer length ( $L_{\text{fibre-reusable}} > L_{\text{fibre-Surgical}} > L_{\text{fibre-N95}}$ , Supplementary Fig. 4d) may have a higher chance to generate a curved structure (higher tortuosity values in Supplementary Fig. 4e), and thus formulate larger diameter pores (over  $65 \mu\text{m}$ ) in sample. We also believe that multiple fabric layers can significantly decrease the momentum of the ejected droplets<sup>18</sup>.

Indeed, in term of general performance, the reusable mask has lowest aerosol filtration and show a higher thermal behaviour ( $T > 27^\circ\text{C}$ ) in Fig. 5a, b, which facilitates  $\text{O}_2$  and  $\text{CO}_2$  to pass through filter since it has the largest pore diameter ( $\Phi_{\text{pore}} = 50 \mu\text{m}$ ). In contrast, the N95 mask offers the best protection among three masks, because the lowest temperature ( $T < 25^\circ\text{C}$ ) was homogeneously captured (Fig. 5e, f), demonstrating a consistent high filtration efficiency when the mask wearer inhales and exhales. Such results provide a solid evidence for previous microstructural analysis. The thermography results

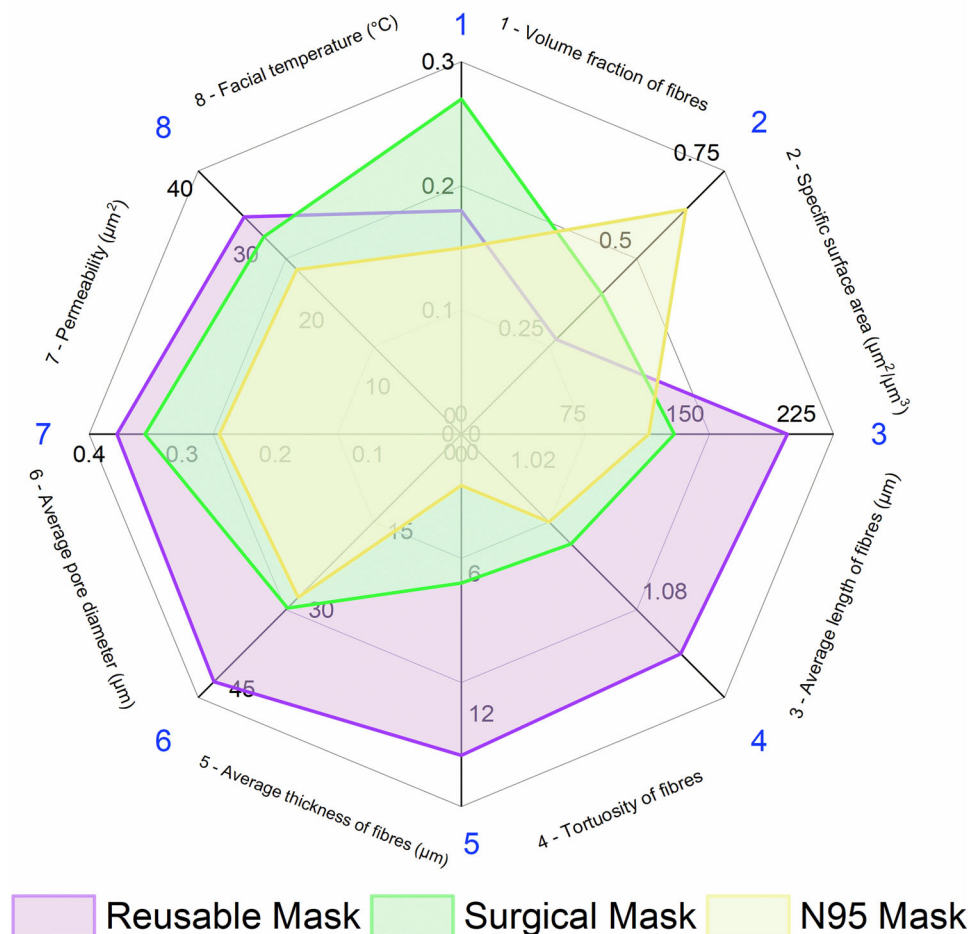


**Fig. 6 The comparison of the microstructures and performance of the three face masks.** The reusable mask has the best breathability and comfortableness (the highest facial temperature, coarse fibres and the largest pore size within fibre spacing) whereas the N95 mask provides the best aerosol filtration (the smallest pore volume, the finest fibres and the largest specific surface area).

(Fig. 5) agree well with droplet flow simulation (Fig. 4), providing an approach to correlate microscale structure with mesoscale performance.

Coupling tomography with the thermography, the relationship between the mask microstructure and performance at mesoscale can be well established in Fig. 6, thus providing scientific evidence for supporting public health guideline. The X-ray imaging generates rich microstructural information which is not obtainable by conventional 2D approaches (i.e., SEM). In Table 2, hundreds of fibres and pores of three face masks are statistically quantified. We believe this study contributes to advancing the current knowledge of the filtration capabilities of the most widely employed face coverings. On the basis of this 3D microstructures analysis, we could contribute to the development of the next generation of N95 masks by tuning its material composition and interior structure to obtain higher filtration efficacy and better breathability. Specifically, we may reduce thickness of Layer #a by 5–20 µm to improve the breathability, while increasing the thickness of Layer #b by 50–150 µm to promote the filtration efficacy. Moreover, adding more homogeneous nanoscale fibres additive in Layer #b will enhance the droplet capture. This knowledge might in turn provide a source of inspiration for the design of functional materials in the face covering fields. For instance, Choi et al.<sup>35</sup> developed a biodegradable, efficient and breathable multi-use face mask filter. Many administrations (i.e., WHO) proposed that wearing a mask

can reduce the risk of virus infections, and we strength this argument with 3D microstructure analysis. All X-ray datasets are made available, freely, in support of this goal.

## Methods

**Selection of specimens.** Three commercial face masks are selected for X-ray investigation: the reusable face mask (Supplementary Fig. 1a), the disposable surgical face mask (Supplementary Fig. 1b) and the N95 stereoscopic face mask with no exhalation valve (Supplementary Fig. 1c) since they are widely commercialised. For simplicity the three masks are termed as the reusable mask, surgical mask and N95 mask, respectively. It should be noted that the three new face masks used in this experiment are anonymous to avoid any conflict of interest. The reusable mask, made by mixing of the polyester, cotton and elastane, is washable and should be washed after every use. The composition can be varied for different mask companies. A small portion of elastane provides the stretching ability. In this study, a single layer mask was used which contains 53% polyester, 45% cotton and 2% elastane. The surgical mask is made by polypropylene (PP) using a melt blowing process. The surgical mask consists of three layers; an inner layer (soft fibres adjacent to the human skin), middle layer (melt-blown filter) and a water-resistant outer layer (nonwoven fibres coloured in blue). The melt-blown filter (in the middle) is the main filtering layer of the surgical mask produced by fabricating micro- and nano-fibres. The N95 mask is also made by PP which has three or four layers. Usually, the nano fabrics of PP will be given an electrostatic charge to enhance the small particle capture ability. The various face mask materials are summarised in Table 4. All samples were trimmed to a smaller size (~3 mm in width) to be easily mounted without any stretching on a sample stage (Supplementary Fig. 1e) for X-ray imaging, thus minimising the elastic effect on pore size quantification.

**Scanning electron microscopy.** Three specimens (including the reusable mask, Layer #2 of surgical mask and Layer #b of N95 mask) were imaged at a working



distance of ca. 8 mm using a Zeiss EVO MA10 (Carl Zeiss AG, Germany) scanning electron microscope (SEM).

**Lab-based X-ray microscale CT.** A lab-based X-ray micro-scale CT scanner (ZEISS Xradia 620 Versa, Carl Zeiss Inc., Pleasanton, USA) was employed to investigate the three samples. The schematic of micro-CT is shown in Supplementary Fig. 1d. This is a non-destructive microscopy technique that allows quantitative analysis of fibrous materials. A polychromatic cone-beam source employing a tungsten target with the voltage set at 40 kV was used. Both 20X and 40X lens were used and the 2048 × 2048 CCD camera detector was binned 1 and 2, respectively (obtaining a detector area of 1024 × 1024 pixel when binning 2 was chosen). Hence, the same voxel resolution at 350 nm with wider (ca. 700 × 700 μm<sup>2</sup>) and narrower (ca. 350 × 350 μm<sup>2</sup>) FOV was achieved for comparison among all specimens. Also, the source-sample and sample-detector distances were adjusted to achieve phase propagation contrast imaging<sup>36</sup> since all masks are made by low-density materials. Projections number ranged from 501 to 1601 were obtained for different specimens. The details of the microscale X-ray imaging parameters for each sample are presented in Table 5.

**X-ray imaging data processing.** We used the standard reconstruction and iterative reconstruction (ZEISS OptiRecon) algorithms to reconstruct projections of three samples within the software (XMReconstructor, Carl Zeiss Inc.). The great novelty of the ZEISS OptiRecon is that using iterative reconstruction provides equivalent results (namely image quality) with fewer projections (typically ¼ of the projections acquired for a conventional scan), thus significantly shortening the image acquisition times. More details can be found in Supplementary Materials.

The reconstructed micro-CT datasets were imported into Avizo 2019.4 software (Thermo Fisher Scientific, USA)<sup>37</sup> for further segmentation and quantification. An unsharp mask filter was applied to sharpen the edges of the fibres without increasing the noise. Three mask samples were then segmented (based on grayscale values) into two phases (fibre and air) using a combination of threshold and watershed methods for general visualisation.

The advanced PNM module in Avizo was applied to the three masks after binarization of filtered datasets. The PNM employed the maximal ball algorithm<sup>37</sup>. Despite the approximations inherent to the network extraction, this method offers a direct approach to study the effect of porosity on air transport, with the overall connectivity of the pore spaces and the microscale behaviour described by pore and throat.

Advanced skeletonization modules (cylinder correlation and trace correlation line)<sup>37</sup> in Avizo (XFibre Extension) were interactively used to detect and track the curved fibrous structures. To extract the fibre length in the sub-volume, three unique templates were created as the fibres of the three masks have different morphological characteristics. This is a robust tool to correctly extract the centerline of fibre structures from binarized images (Fig. 3, first column), but artefacts might occur at a region near a boundary. The statistical quantification of fibre length and correlated pore diameter using the skeletonization and PNM is summarised in Table 2.

**Image-based simulation.** The absolute permeability ( $\chi$ ) along the Z-axis direction (perpendicular to mask plane) was calculated in Avizo XLab Hydro (an image-based model based on the Stokes' equations). This helps to understand how aerosol containing bacteria and coronaviruses penetrates the mask, thus evaluating the air filtration performance of the three face masks. A sub-volume (460 × 460 × 100 voxel<sup>3</sup>) was extracted from the entire volumetric tomogram to minimise the computational effort. To carry out a direct comparison between the three specimens, the same sub-volumes (161 × 161 × 35 μm<sup>3</sup>) were cropped for all specimens. The assumptions and the boundary conditions for modelling were as follows: no volume changes and the entire sample environment remains unchanged (i.e., w.r.t. moisture); the flow rate was set as 5.6 × 10<sup>11</sup> μm<sup>3</sup> s<sup>-1</sup>. The droplet flow velocity is 10 ~ 25 × 10<sup>6</sup> μm s<sup>-1</sup> when an individual coughs<sup>38</sup>, and an intermediate value (20 × 10<sup>6</sup> μm s<sup>-1</sup>) was applied in this study. The output pressures were then set as 0.01 Pa since the aerosol reaches skin if aerosol passes through a filter. The air viscosity at 15 °C was set to be the same (1.8 × 10<sup>-5</sup> Pa s) according to ref. <sup>39</sup>.

**IR thermal imaging.** The thermal behaviour of face masks was evaluated in real-time during breathing inhalation and exhalation using an IR thermal camera (FLIR One Pro LT, USA) with a frame rate of 8.7 Hz. The distance between the thermal camera and the mask wearer was fixed at 25 cm. The thermal and visual resolution of the thermal camera were 80 × 60 and 1440 × 1080 pixels, respectively. The thermal camera has been designed to be compatible with smartphones, thus it will be a fast approach to perform breathability test for commercial face masks. The authors affirm that informed consent for publication of the images in Fig. 5 was obtained from the identifiable individual.

## Data availability

All datasets needed to evaluate the conclusions are presented in the paper included Figures and Supplementary Movies. Additional data related to this paper may be requested from the authors for educational and academic purposes. All raw X-ray

tomography files are available at the University College London Research Data Repository (<https://doi.org/10.5522/04/13308485>, <https://doi.org/10.5522/04/13308611> and <https://doi.org/10.5522/04/13308488>).

Received: 14 January 2021; Accepted: 20 April 2021;  
Published online: 22 June 2021

## References

- Sohrabi C. et al. World Health Organization declares global emergency: A review of the 2019 novel coronavirus (COVID-19). *Int. J. Surg.* **76**, 71–76 (2020).
- Ranney, M. L., Griffeth, V. & Jha, A. K. Critical supply shortages—the need for ventilators and personal protective equipment during the Covid-19 pandemic. *N. Engl. J. Med.* **382**, e41 (2020).
- Johns Hopkins University. Johns Hopkins CSSE Covid-19 Dashboard <https://coronavirus.jhu.edu/map.html> (2021).
- Anderson, R. M., Heesterbeek, H., Klinkenberg, D. & Hollingsworth, T. D. How will country-based mitigation measures influence the course of the COVID-19 epidemic? *Lancet* **395**, 931–934 (2020).
- Hellewell, J. et al. Feasibility of controlling COVID-19 outbreaks by isolation of cases and contacts. *Lancet Glob. Health* **8**, e488–e496 (2020).
- Bedford, J. et al. COVID-19: towards controlling of a pandemic. *Lancet* **395**, 1015–1018 (2020).
- Ministry of Health Singapore. Guidance for use of masks and face shields. *MOH* (1 June 2020).
- Mills M, Rahal C, Akimova E. Face masks and coverings for the general public: behavioural knowledge, effectiveness of cloth coverings and public messaging. (The Royal Society & The British Academy 2020).
- Chu, D. K. et al. Physical distancing, face masks, and eye protection to prevent person-to-person transmission of SARS-CoV-2 and COVID-19: a systematic review and meta-analysis. *Lancet* **395**, 1973–1987 (2020).
- Leung, N. H. L. et al. Respiratory virus shedding in exhaled breath and efficacy of face masks. *Nat. Med.* **26**, 676–680 (2020).
- Eikenberry, S. E. et al. To mask or not to mask: modeling the potential for face mask use by the general public to curtail the COVID-19 pandemic. *Infect. Dis. Model.* **5**, 293–308 (2020).
- Leung, C. C., Lam, T. H. & Cheng, K. K. Mass masking in the COVID-19 epidemic: people need guidance. *Lancet* **395**, 945 (2020).
- Feng, S. et al. Rational use of face masks in the COVID-19 pandemic. *Lancet Resp. Med.* **8**, 434–436 (2020).
- Greenhalgh, T., Schmid, M. B., Czypionka, T., Bassler, D. & Gruer, L. Face masks for the public during the covid-19 crisis. *BMJ* **369**, m1435 (2020).
- BBC. Hundreds at Sheffield anti-mask coronavirus protest <https://www.bbc.co.uk/news/uk-england-south-yorkshire-54043103> (2020).
- Lam, T. N. et al. Multi-scale microstructure investigation for a PM2.5 air-filter efficiency study of non-woven polypropylene. *Quant. Beam Sci.* **3**, 20 (2019).
- Fischer, E. P. et al. Low-cost measurement of face mask efficacy for filtering expelled droplets during speech. *Sci. Adv.* **6**, eabd3083 (2020).
- Aydin, O. et al. Performance of fabrics for home-made masks against the spread of COVID-19 through droplets: a quantitative mechanistic study. *Extreme Mech. Lett.* **40**, 100924 (2020).
- Wang, D. et al. Can masks be reused after hot water decontamination during the COVID-19 pandemic? *Engineering* **6**, 1115–1121 (2020).
- Mehta, P. et al. Engineering optimisation of commercial facemask formulations capable of improving skin moisturisation. *Int. J. Cosmet. Sci.* **41**, 462–471 (2019).
- Lee, H. R. et al. Three-dimensional analysis of particle distribution on filter layers inside N95 respirators by deep learning. *Nano Lett.* **21**, 651–657 (2020).
- Dong, H. & Blunt, M. J. Pore-network extraction from micro-computerized-tomography images. *Phys. Rev. E* **80**, 036307 (2009).
- Diamond Sidney. Mercury porosimetry: an inappropriate method for the measurement of pore size distributions in cement-based materials. *Cem. Concr. Res.* **30**, 1517–1525 (2000).
- Rutledge, G. C., Lowery, J. L. & Pai, C. L. Characterization by mercury porosimetry of nonwoven fiber media with deformation. *J. Eng. Fibers Fabr.* **4**, 155892500900400301 (2009).
- Withers, P. J. et al. X-ray computed tomography. *Nat. Rev. Methods Primers* **1**, 1–21 (2021).
- Gharedaghlou, B., Price, J. S., Rezanezhad, F. & Quinton, W. L. Evaluating the hydraulic and transport properties of peat soil using pore network modeling and X-ray micro computed tomography. *J. Hydrol.* **561**, 494–508 (2018).
- Wang, J. Q. et al. Permeability of laboratory-formed porous media containing methane hydrate: observations using X-ray computed tomography and simulations with pore network models. *Fuel* **145**, 170–179 (2015).

28. Han, Z. Y., Weng, W. G. & Huang, Q. Y. Characterizations of particle size distribution of the droplets exhaled by sneeze. *J. R. Soc. Interface* **10**, 20130560 (2013).
29. Xie, X., Li, Y., Sun, H. & Liu, L. Exhaled droplets due to talking and coughing. *J. R. Soc. Interface* **6**, S703–S714 (2009).
30. Loudon, R. G. & Roberts, R. M. Droplet expulsion from the respiratory tract. *Am. Rev. Respir. Dis.* **95**, 435–442 (1967).
31. Buckland, F. E. & Tyrrell, D. A. J. Experiments on the spread of colds: 1. Laboratory studies on the dispersal of nasal secretion. *Epidemiol. Infect.* **62**, 365–377 (1964).
32. Cheng, C. H., Chow, C. L. & Chow, W. K. Trajectories of large respiratory droplets in indoor environment: a simplified approach. *Build. Environ.* **183**, 107196 (2020).
33. Xie, X., Li, Y., Chwang, A. T. Y., Ho, P. L. & Seto, W. H. How far droplets can move in indoor environments—revisiting the Wells evaporation–falling curve. *Indoor Air* **17**, 211–225 (2007).
34. Wang, C. S. Electrostatic forces in fibrous filters—a review. *Powder Technol.* **118**, 166–170 (2001).
35. Choi, S., et al. Biodegradable, efficient, and breathable multi-use face mask filter. *Adv. Sci.* **8**, 2003155 (2021).
36. Endrizzi, M. X-ray phase-contrast imaging. *Nucl. Instrum. Methods Phys. Res. A* **878**, 88–98 (2018).
37. ThermoFisher Scientific. Avizo Software User’s Guide. <https://assets.thermofisher.com/TFS-Assets/MSD/Product-Guides/user-guide-avizo-software.pdf> (2019).
38. Mittal, R., Ni, R. & Seo, J. H. The flow physics of COVID-19. *J. Fluid Mech.* **894**, 1–14 (2020).
39. Lemmon, E. W. & Jacobsen, R. T. Viscosity and thermal conductivity equations for nitrogen, oxygen, argon, and air. *Int. J. Thermophys.* **25**, 21–69 (2004).

## Acknowledgements

This COVID-19 related investigation was established in consultation with Prof Rebecca Shipley, UCL Institute for Healthcare Engineering. We thank Dr Josh Bailey for providing the IR thermal camera and the assistance of Dr Zhenyu Zhang. We would like to acknowledge the grant from the EPSRC grant for supporting the emerging energy works in the Electrochemical Innovation Lab (EP/R020973/1 and EP/S018204/1) and the X-ray instruments (EP/K005030/1). P.R.S acknowledges funding from The Royal Academy of Engineering (CiET1718/59).

## Author contributions

W.D. and F.I. conducted the experiments and project administration. W.D. performed the formal analysis and original manuscript writing. T.F. and R.L. procured the masks and consultation. D.J.L.B. and P.R.S. supervised the project, manuscript edit and funding acquisition. All authors were involved in data interpretation and manuscript preparation.

## Competing interests

The authors declare no competing interests.

## Additional information

**Supplementary information** The online version contains supplementary material available at <https://doi.org/10.1038/s43246-021-00160-z>.

**Correspondence** and requests for materials should be addressed to P.R.S.

**Peer review information** Primary handling editor: John Plummer.

**Reprints and permission information** is available at <http://www.nature.com/reprints>

**Publisher’s note** Springer Nature remains neutral with regard to jurisdictional claims in published maps and institutional affiliations.



**Open Access** This article is licensed under a Creative Commons Attribution 4.0 International License, which permits use, sharing, adaptation, distribution and reproduction in any medium or format, as long as you give appropriate credit to the original author(s) and the source, provide a link to the Creative Commons license, and indicate if changes were made. The images or other third party material in this article are included in the article’s Creative Commons license, unless indicated otherwise in a credit line to the material. If material is not included in the article’s Creative Commons license and your intended use is not permitted by statutory regulation or exceeds the permitted use, you will need to obtain permission directly from the copyright holder. To view a copy of this license, visit <http://creativecommons.org/licenses/by/4.0/>.

© The Author(s) 2021